

Accepted Manuscript

A novel approach to fabricate carbon-sphere-intercalated holey graphene electrode for high-energy-density electrochemical capacitors

Shuxing Wu, Kwan San Hui, Kwun Nam Hui, Je Moon Yun, Kwang Ho Kim

PII: S1385-8947(17)30197-3
DOI: <http://dx.doi.org/10.1016/j.cej.2017.02.040>
Reference: CEJ 16479

To appear in: *Chemical Engineering Journal*

Received Date: 26 October 2016
Revised Date: 19 January 2017
Accepted Date: 7 February 2017

Please cite this article as: S. Wu, K. San Hui, K. Nam Hui, J. Moon Yun, K. Ho Kim, A novel approach to fabricate carbon-sphere-intercalated holey graphene electrode for high-energy-density electrochemical capacitors, *Chemical Engineering Journal* (2017), doi: <http://dx.doi.org/10.1016/j.cej.2017.02.040>

This is a PDF file of an unedited manuscript that has been accepted for publication. As a service to our customers we are providing this early version of the manuscript. The manuscript will undergo copyediting, typesetting, and review of the resulting proof before it is published in its final form. Please note that during the production process errors may be discovered which could affect the content, and all legal disclaimers that apply to the journal pertain.



**A novel approach to fabricate carbon-sphere-intercalated holey graphene electrode
for high-energy-density electrochemical capacitors**

Shuxing Wu ^a, Kwan San Hui ^{b,*}, Kwun Nam Hui ^{c,*}, Je Moon Yun ^d, Kwang Ho Kim ^{a, d,*}

^aSchool of Materials Science and Engineering, Pusan National University, San 30 Jangjeon-dong, Geumjeong-gu, Busan 609-735, Republic of Korea

^bSchool of Mathematics, University of East Anglia, Norwich, NR4 7TJ, United Kingdom

^cInstitute of Applied Physics and Materials Engineering, University of Macau, Avenida da Universidade, Taipa, Macau, China

^dGlobal Frontier R&D Center for Hybrid Interface Materials, Pusan National University, 30 Jangjeon-dong, Geumjung-gu, Busan 609-735, South Korea

**Corresponding author:*

E-mail: bizhui@umac.mo (Kwun Nam Hui)

Email: k.hui@uea.ac.uk (Kwan San Hui)

E-mail: kwhokim@pusan.ac.kr (Kwang Ho Kim)

ABSTRACT

Desirable porous structure and huge ion-accessible surface area are crucial for rapid electronic and ionic pathway electrodes in high-performance graphene-based electrochemical capacitors. However, graphene nanosheets tend to aggregate and restack because of van der Waals interaction among graphene sheets, resulting in the loss of ion-accessible surface area and unsatisfactory electrochemical performance. To resolve this daunting challenge, a novel approach is developed for the self-assembly of holey graphene sheets intercalated with carbon spheres (H-GCS) to obtain freestanding electrodes by using a simple vacuum filtration approach and a subsequent KOH activation process. Through the introduction of carbon spheres as spacers, the restacking of reduced graphene oxide (rGO) sheets during the filtration process is mitigated efficiently. Pores on rGO sheets produced by subsequent KOH activation also provide rapid ionic diffusion kinetics and high ion-accessible electrochemical surface area, both of which favor the formation of electric double-layer capacitance. Furthermore, a higher degree of graphitization of CSs in H-GCS thin film improves the electrical conductivity of the H-GCS electrode. The H-GCS electrode exhibits 207.1 F g^{-1} of specific capacitance at a current density of 1 A g^{-1} in 6 M KOH aqueous electrolyte. Moreover, the symmetric electrochemical capacitor assembled with H-GCS electrodes and organic electrolyte is capable of delivering a maximum energy density of 29.5 Wh kg^{-1} and a power density of 22.6 kW kg^{-1} .

Keywords: Electrochemical capacitor; High-energy-density; Holey graphene; Carbon sphere

1. Introduction

Electric double-layer capacitors (EDLCs) are attractive energy storage devices for applications where high power densities and long cycle life are key desirable parameters [1, 2]. Unlike batteries that are restricted by slow chemical reactions, EDLCs can store energy through fast and reversible ion adsorption/desorption reaction at the electrode–electrolyte interface [3-5]. To sustain fast and reversible electrochemical interactions, electrode materials should possess large ion-accessible surface areas and efficient transport pathways for ions and electrons [6]. Importantly, high conducting and binder-free electrodes are critical conditions to achieve high-energy-density EDLCs. The addition of conductive additives and binders leads to undesirably low active-to-substrate mass ratio, low electrolyte penetration, decreased conductivity, and increased total mass [7-9].

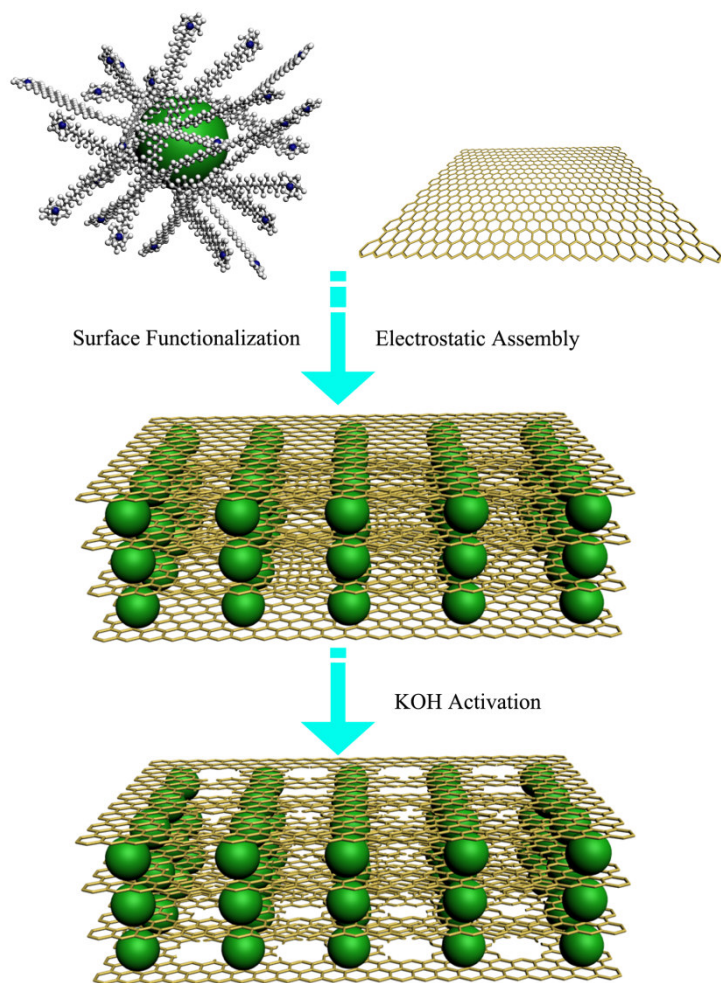
Graphene, a two-dimensional (2D) monolayer of carbon atoms packed into a honeycomb lattice, is a promising building block for realizing high-power-density and long-cycle-life EDLCs owing to its exceptionally enormous high surface area (theoretically, over $2630 \text{ m}^2 \text{ g}^{-1}$ per single layer), high intrinsic electrical conductivity, excellent mechanical flexibility, and high chemical stability [10-12]. Another merit of graphene as a promising electrode in EDLCs is that both surfaces of a graphene sheet are exterior surfaces, which are readily accessible for the electrolyte [13]. Given that the total theoretical surface area of graphene is fully utilized, a galvanostatic specific capacitance value of up to 550 F g^{-1} can be achieved [14]. Owing to the ease of preparation and processing from abundant and low-cost graphite, graphene is now being manufactured on the ton scale at low cost [15]. However, this chemically derived graphene is a defect-rich material compared with

models based on theoretical calculations [16, 17]. Another daunting challenge in fully utilizing 2D graphene as electrodes in supercapacitors includes aggregation and restacking of graphene sheets because of the van der Waals interaction among graphene sheets. This limitation severely decreases the electrochemically active surface area and precludes the access of electrolyte ions to the surface of graphene sheets. Consequently, capacitive performance is diminished drastically, particularly the rate capability and cycling stability [18, 19]. The origin of the aggregation is attributed to the van der Waals attraction between graphene layers, an attraction that is proportional to the overlapping area (S) and the fourth power of the inverse of interlayer space between sheets ($1/d^4$) [20, 21]. Owing to their high aspect ratio, graphene sheets are soft and prone to forming conformal contact with a surface or with each other, thereby significantly increasing S and reducing d and leading to a strong attraction [20]. Owing to the advantages of pseudocapacitance arising from other constituents, several research approaches have been devoted to minimize aggregation and restack graphene sheets by hybridizing graphene with carbonaceous materials, metal oxide/hydroxides, and polymers [22-32].

Accordingly, one-dimensional carbon nanotubes (CNTs) have been extensively studied and adopted as a smart spacer among graphene sheets because CNTs can effectively serve as electrical conducting paths while preventing the graphene from aggregation [33-38]. However, CNTs remain expensive and suffer from drawbacks of a tedious fabrication process. From a perspective of environmental protection and sustainable development, carbon-based materials derived from nature using a facile yet economic synthesis procedure are highly desirable. Alternatively, a self-assembled hierarchical nanostructure comprising carbon spheres (CSs) synthesized by hydrothermal

carbonization of glucose and graphene sheet has been demonstrated to alleviate the aggregation of graphene [39]. Although studies [3, 39, 40] have demonstrated the promise of graphene/CSs electrode in achieving high-performance EDLCs, the electrochemical performance of corresponding EDLCs is still low because of i) the addition of an organic binder, which causes “dead” volume effect; ii) the absence of pores in the graphene layers, resulting in inferior ion diffusion; and iii) the presence of oxygen-containing groups due to incomplete reduction, which largely degrades electrical conductivity. In the current report, an approach to fabricate a high electrical conducting and porous architecture consisting of holey graphene sheets intercalated with carbon spheres (H-GCS) is developed via hydrazine reduction, vacuum filtration, and subsequent KOH activation (Scheme 1). First, CSs are fully cladded and bridged by reduced graphene oxide (rGO) sheets, which are formed by electrostatic attractive interactions between negatively charged rGO sheets and positively charged CSs functionalized by a cationic surfactant. In this approach, CSs play an important role as spacers to prevent graphene from self-restacking and render the formation of unique 3D heterostructure architectures. The merits of the CS spacers greatly increase electrolyte-accessible surface area and enhance the utilization efficiency of graphene. Second, KOH activation of the as-synthesized GCS structures under an inert atmosphere (Ar) not only can effectively yield holey graphene, further reduce oxygen-containing groups, but also promote the graphitization of amorphous CSs between rGO sheets, leading to an enhanced conductivity. Thus, both high electrical conductivity and porosity of the H-GCS electrode can be obtained simultaneously, which is critical for high rate capability and rapid ion transportation [41]. As a proof of concept, the electrochemical performance of the proposed H-GCS structure

is characterized and its applications as electrodes for symmetric EDLCs are presented. The intrinsic flexibility of such H-GCS thin films renders its use as a binder-free electrode directly. Electrochemical measurement on the H-GCS thin films are carried out in symmetric devices (coin cells, CR 2302) with 1 M tetraethylammonium tetrafluoroborate (TEABF₄) in acetonitrile (AN) as electrolyte. Without using any auxiliary additives, freestanding H-GCS electrode exhibits high specific gravimetric capacitance of 94.3 F g⁻¹ in the organic electrolyte with 3 V voltage window at a current density of 1 A g⁻¹, as well as stable capacitance retention of 85.0% over a wide range of current densities from 1 to 15 A g⁻¹. Symmetric capacitor consists of H-GCS//H-GCS that delivers a maximum energy density of 29.5 Wh kg⁻¹ at a maximum power density of 22.6 kW kg⁻¹. The unique H-GCS electrode likewise exhibits long-term cycling stability with 79% of capacitance retention after 5000 cycles.



Scheme 1. Schematic illustration of the carbon sphere-intercalated holey graphene 3D heterostructured architectures. Electrostatic attractive interactions between negatively charged rGO sheets and positively charged CTAB-grafted carbon spheres render the formation of 3D heterostructured architectures. KOH activation produces pores in the graphene layers, which are expected to provide rapid ion diffusion path.

2. Experimental

2.1. Synthesis of rGO colloid and CSs

Flake graphite (Asbury Carbons) was first oxidized by a modified Hummer's method to obtain graphite oxide [42, 43]. Briefly, 3 g of graphite flakes were stirred in concentrated sulfuric acid (H_2SO_4 , 70 mL) at room temperature (RT), and then sodium nitrate (NaNO_3 , 1.5 g) was added. While keeping the reaction flask in an ice bath, potassium permanganate (KMnO_4 , 9.0 g) was added slowly into the suspension, and the temperature of the suspension was kept below 20 °C. Next, the reaction system was placed in a 35 °C water bath for 30 min, which resulted in the formation of a slurry. Subsequently, 140 mL deionized (DI) water was added, and the suspension was stirred for another 15 min. Finally, DI water (500 mL) and hydrogen peroxide solution (H_2O_2 , 30 wt %, 20 mL) were slowly added to obtain a yellow graphite oxide solution. This solution was filtered and washed with 1:10 HCl aqueous solution (250 mL), followed by repeated washing with DI water and centrifugation. The solution was freeze-dried to obtain a brownish graphite oxide powder. The resulting graphite oxide was dispersed in DI water by ultrasonication to make a graphene oxide (GO) aqueous dispersion (0.25 mg mL^{-1}), which was then subjected to 30 min centrifugation at 4000 rpm to remove any unexfoliated graphite oxide. The above suspension was adjusted to pH 10–10.5 by ammonia solution (28 wt% in water) followed by the addition of a hydrazine solution (35 wt% in water, mass ratio hydrazine/graphene oxide = 7:10) to reduce GO.

The CSs were fabricated via hydrothermal reaction in a stainless steel autoclave (50 mL in total capacity) under autogenous pressure. In the typical process, 4 g of glucose was dissolved in 40 mL of DI water, and then the solution was transferred to the autoclave. The autoclave was sealed and maintained at 180 °C for 4 h. After being cooled naturally

to RT, the products were collected and washed with DI water and ethanol several times followed by drying at 80 °C in air.

2.2. Synthesis of GCS papers

GCS paper was fabricated through a self-assembly method via electrostatic interaction between negatively charged rGO and positively charged CSs. The positively charged CSs were functionalized with a cationic surfactant (cetyltrimethylammonium bromide: CTAB). First, CTAB was dissolved in DI water (1 wt%), and CSs powder was added. The resulting dispersion was stirred for 5 h and excess CTAB was removed by centrifugation/washing/redispersion. Next, 30 mL of functionalized CSs aqueous dispersion (pH 9.5) was added into 70 mL of rGO solution under gentle stirring at RT (mass ratio GO/CSs = 10/1). After 2 h, the mixture was vacuum-filtered over a polytetrafluoroethylene membrane (0.2 μm pore size, 47 mm in diameter; SciLab) to form a homogeneous thin film, and a free-standing film was carefully peeled off from the filter membrane.

2.3. Synthesis of H-GCS

The as-prepared GCS thin film was infiltrated in 20 mL KOH solution (2 M) for 24 h in ambient conditions, and the thin film was taken out of the KOH solution and dried at 60 °C for 12 h. The activation process was operated at 800 °C for 1 h in a horizontal tube furnace under argon atmosphere. The temperature was ramped to 800 °C at 5 °C min^{-1} . After cooling, the sample was repeatedly washed with 1 M HCl and DI water until pH 7 was reached. Finally, the H-GCS thin film was dried at 60 °C for 12 h.

2.4. Assembling of coin-cell supercapacitor devices

The coin-cell devices were assembled in an argon-filled glove box using the CR 2032 cell case [44]. The samples were punched into round electrodes 15 mm in diameter. The stacking sequence of the coin cell consisted of the bottom cap, gasket, spacer, electrode disk, polypropylene separator (17 mm), electrode disk, electrolyte (1 M TEABF₄ in AN), spacer, spring, and top cap. The mass loading of the H-GCS electrode was 0.47 mg cm⁻².

2.5. Characterization

X-ray powder diffraction (XRD) patterns were collected on a Rigaku MPA-2000 X-ray diffractometer with Cu α radiation ($\lambda = 1.5418 \text{ \AA}$) at 40 kV voltage and a current of 40 mA. The microstructures were characterized under scanning electron microscopy (SEM, Tescan MIRA3 LMH) and transmission electron microscopy (TEM, FEI Talos, USA). X-ray photoelectron spectroscopy (XPS) measurements were performed via the Thermo VG Escalab 250 photoelectron spectrometer. Raman spectra of the samples were recorded at room temperature using a Jobin-Yvon Horiba HR800 UV Raman microscope. This instrument used a 514 nm laser as excitation source. Tapping-mode atomic force microscopy (AFM) images were obtained via the Nanoscope IIIa Multimode instrument (Digital Instruments, California). The electrical conductivity was tested by a four point probe setup (Ecopia, HMS-3000). The nitrogen absorption/desorption isotherms were obtained with a commercial manometric device (nanoPOROSITY-XQ, Mirae Scientific Instruments Co., Korea). The specific surface area (SSA) was calculated from nitrogen isotherms using the Brunauer-Emmett-Teller (BET) equation. The pore size distributions were determined by applying the Barrett-Joyner-Halenda (BJH) method.

2.6. Electrochemical measurements

Electrochemical properties and results were determined using an IviumNstat electrochemical station. Three-electrode tests were performed in a 6 M KOH electrolyte with saturated calomel electrode (SCE, Hg/Hg₂Cl₂) as the reference electrode and platinum foil as the counter electrode. Thin-film samples (1 × 1 cm²) were used directly as working electrodes. The specific capacitance derived from galvanostatic charge-discharge (GCD) tests was calculated using the following equation:

$$C_s = I \times \Delta t / (\Delta V \times m) \quad (1)$$

where C_s (F g⁻¹), I (A), Δt (s), ΔV , and m (g) are the specific capacitance, discharge current, discharge time, potential window (here, $\Delta V = 1$ V), and mass of the thin-film samples, respectively. Cyclic voltammetry (CV) and GCD for symmetric SCs were obtained from 0 V to 3 V. The cycle life tests were conducted by using GCD measurements with a constant current density of 5 A g⁻¹ for 5000 cycles. The total gravimetric capacitance (C_t) of a supercapacitor cell was calculated from GCD process as follows:

$$C_t = I \times \Delta t / (\Delta V \times M) \quad (2)$$

where I is the instant current, ΔV represents the voltage drop on discharging after the IR drop, Δt is the time for a full discharge, and M is the total mass of the thin-film materials in two electrodes. In symmetric supercapacitors, the specific capacitance (C_{sc}) of the electrodes was calculated from Equation (3):

$$C_{sc} = 4 C_t \quad (3)$$

Energy and power densities were calculated using the following equations:

$$E = \frac{1}{2} \times C_t \times \Delta V^2 \quad (4)$$

$$P = E/\Delta t \quad (5)$$

3. Results and discussion

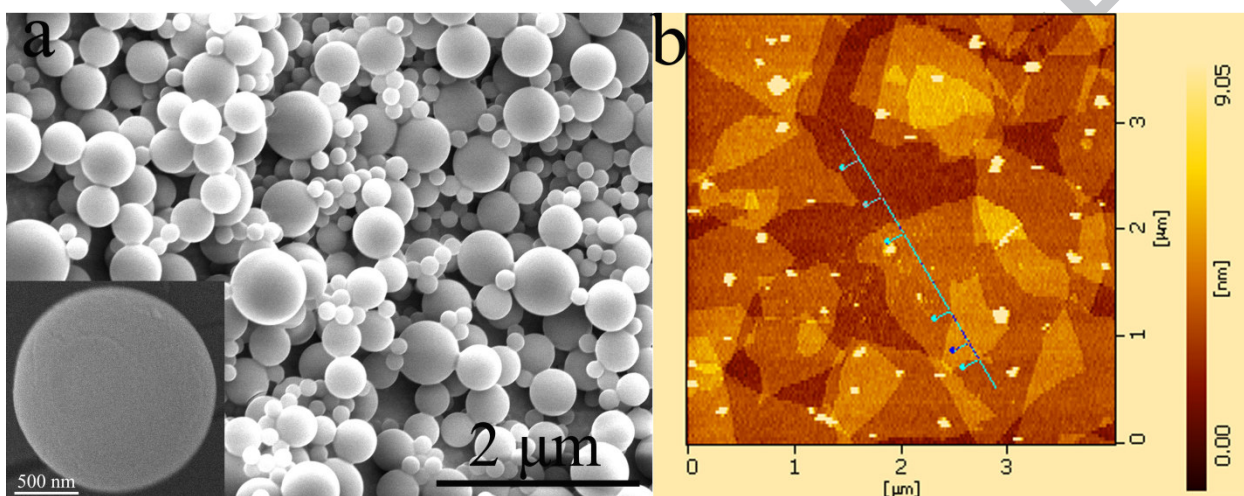


Fig. 1. (a) SEM images of CSs and (b) Tapping mode AFM image of GO sheets deposited on SiO₂ substrate.

Fig. 1a shows the SEM image of CSs obtained by hydrothermal carbonization of D-glucose at 180 °C. The images indicated that the as-prepared CSs with smooth surfaces have a size range of 1–6 μm. These CSs did not form aggregation. According to previous research, CSs are mainly polysaccharides containing abundant –OH and C=O groups on their surface, which facilitate the functionalization with CTAB and the dispersion in DI water [45, 46]. Fig. 1b shows an AFM image of GO sheets. The thickness of the flat GO sheets is ~1.1 nm. The size demonstrates the full exfoliation of graphite oxide (Fig. S1) and is consistent with the predicted effective single-sheet thickness for GO [47]. Rational synthesis and self-assembly of GCS were developed through electrostatic interactions between CSs and rGO. Negatively charged rGO colloids exhibited Zeta potential of -

40.0 mV at pH 9.5 (Fig. S2b) because of the presence of carboxylic acid (COOH^-) [48]. Positively charged CSs at pH 9.5 (Fig. S2d) were obtained by functionalizing with a cationic surfactant (CTAB) [37, 49].

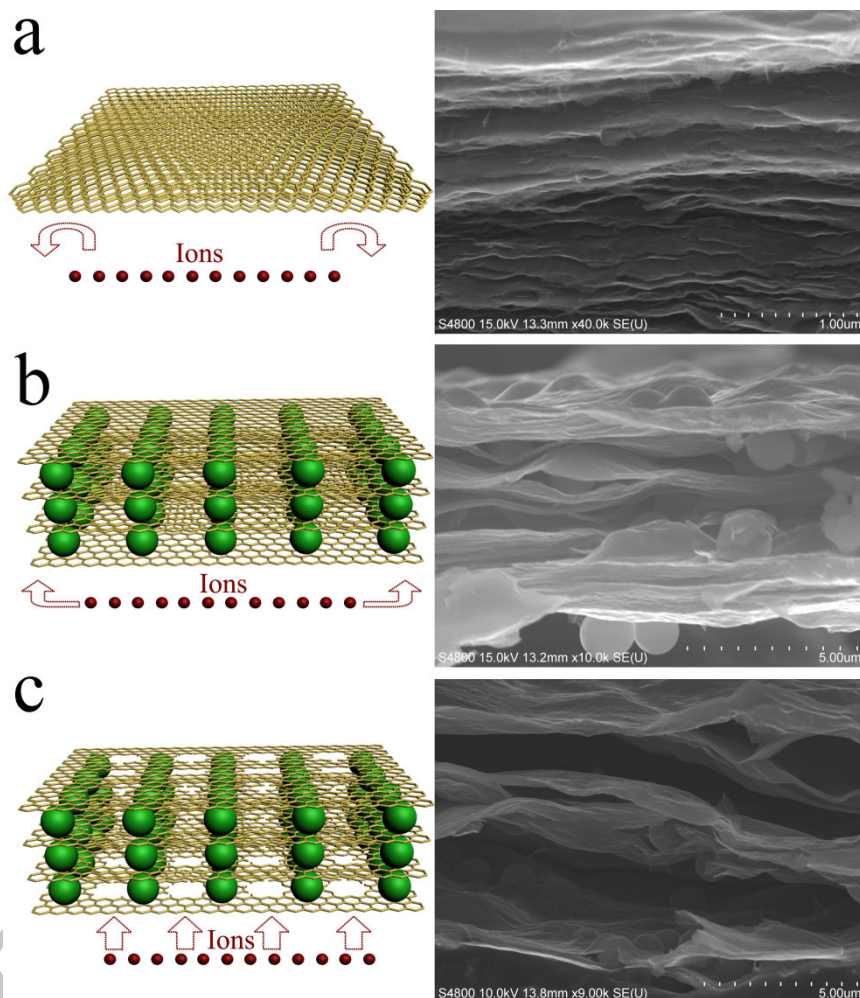


Fig. 2. Schematic illustration and cross-sectional SEM images of (a) rGO, (b) GCS, and (c) H-GCS thin films. (a) Original rGO thin film without CSs. The individual rGO sheets are prone to self-restacking because of the van der Waals interactions, leading to the inferior migration behavior of electrolyte ions between the restacked rGO sheets. (b) rGO

sheets intercalated by CS with large inter-layer voids, leaving more diffusion pathways for electrolyte ions. (c) Holes in the pillared rGO sheets can function as the ion transport pathways to speed up ion migration through the entire H-GCS film.

Fig. 2 shows the typical cross-sectional SEM images of plain rGO, GCS, and H-GCS thin films along with their schematic illustrations. Pristine rGO film (has a thickness of about 1.7 μm) displayed a densely compacted layered structure, suggesting that rGO sheets tended to self-assemble repeatedly under the vacuum filtration-induced directional flow (Fig. 2a). By contrast, GCS film ($\sim 5.9 \mu\text{m}$ thick) exhibited a loose structure and possessed numerous cavities (Fig. 2b), which are good for electrolyte diffusion and applicable for supercapacitors. After KOH chemical activation, the structure was well retained and the thickness was increased to $\sim 7.5 \mu\text{m}$ (Fig. 2c). The activation of graphene with KOH proceeds as $6\text{KOH} + \text{C} \leftrightarrow 2\text{K} + 3\text{H}_2 + 2\text{K}_2\text{CO}_3$, in which KOH is reduced by graphene to metallic potassium and the graphene is etched to give rise to the porosity [50]. Furthermore, vapors of potassium metal were intercalated between the graphene layers, causing swelling of the carbon microstructure and thereby generating additional porosity [51]. These pores can effectively facilitate ion transport kinetics by providing shorter diffusion pathways while offering a larger electrochemical surface area.

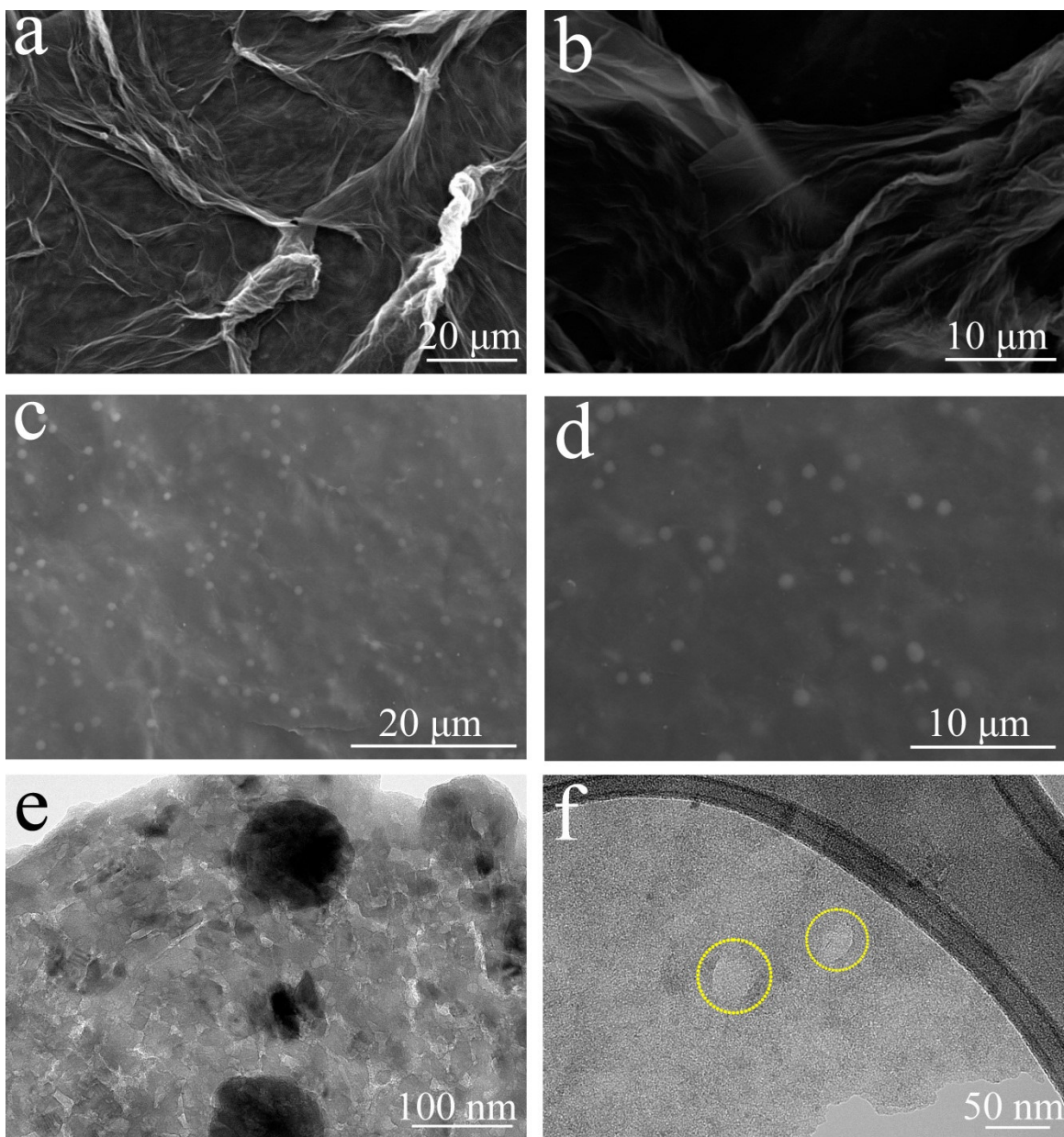


Fig. 3. Top-view SEM images of rGO (a and b) and GCS (c and d), and TEM images of H-GCS (e and f) thin films.

Fig. 3 shows the top-view SEM images of plain rGO and GCS and TEM images of H-GCS. Their corresponding thin film fabricated by a simple vacuum filtration process (Fig. S3). Plain rGO thin film, without the incorporation of CSs into rGO sheets, presents the wrinkled structure and severe aggregation and restacking phenomenon, where rGO sheets

overlapped with each other (Fig. 3a and b). By contrast, graphene sheets with laminar morphology-like silk veil waves were observed (Fig. 3c and d) [39]. These results indicated a strong interaction between rGO and CSs, where CSs are spaced between rGO sheets to form a 3D network and alleviate the aggregation and restacking of rGO sheets. The advantages of the proposed GCS architecture include the following: 1) continuous rGO sheets can favor electron transport, 2) intercalated CSs can prevent the rGO sheet from restacking, and 3) intrinsic wrinkles and ripples on the graphene surface can offer additional flexibility for film deformation. Fig. 3e and S4 show the TEM images of the the H-GCS sample. As observed, CSs are supported onto the graphene sheets and large quantities of mesopores can be observed. A high-resolution TEM image of the H-GCS (Fig. 3f) demonstrates that numerous micropores are homogeneously distributed. In addition, mesopores (as marked by dashed circles) are clearly observed. Such a holey structure can effectively provide more electroactive sites, facilitate the effective accessibility of electrolyte ions, and accommodate volume changes during charge and discharge for SC applications [52, 53]. The porous nature of the H-GCS samples was also characterized by nitrogen adsorption/desorption measurement (Figure S5). Before the measurement, the thin film samples were cut into small pieces. Based on the BET method, the SSA of rGO, GCS, and H-GCS thin films are 54.83, 129.77, and 288.19 $\text{m}^2 \text{g}^{-1}$, respectively. The obtained multimodal pore size distribution for rGO, GCS, and H-GCS thin films are present in Fig. S5b, c and d. Results show that the rGO and GCS thin films possess pore sizes ranging between 2 and 10 nm. The results confirm that mesopores were generated by the KOH treatment. It is clear that the H-GCS films possess the highest SSA, largest quantities of mesopores and largest total pore volume compare to the

rGO and GCS films. Based on the results of SEM, TEM, and nitrogen adsorption/desorption isotherm, the H-GCS films demonstrate a hierarchical holey structure with numerous micro-mesopores. Therefore, the proposed H-GCS films exhibit high BET SSA and well-developed micro-mesopores, which are believed to be extremely beneficial for energy storage applications.

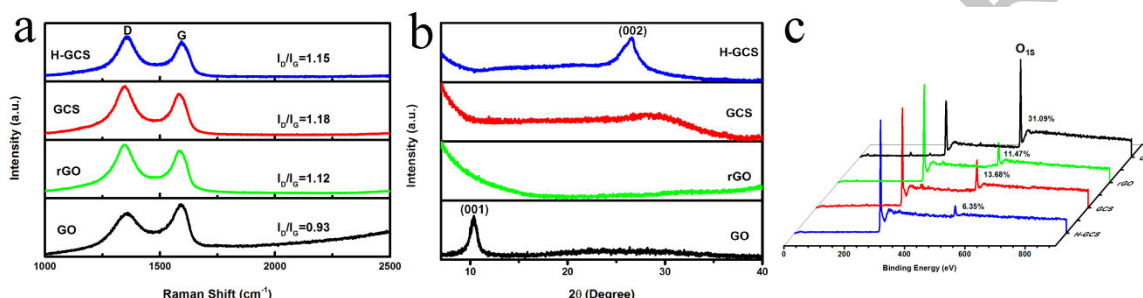


Fig. 4. (a) Raman spectra, (b) XRD patterns and (c) XPS spectra of GO, rGO, GCS, and H-GCS

Fig. 4a shows the Raman spectra for GO, rGO, GCS, and H-GCS, all of which revealed a pronounced D band at around 1350 cm^{-1} and a G band at around 1580 cm^{-1} . The D band is associated with structural defects or a partially disordered structure of graphitic domains, while the G band corresponds to the first-order scattering of E_{2g} mode of sp^2 carbon atoms in the hexagonal carbon framework [54]. The I_D/I_G ratio calculated from the Raman spectrum can be utilized as an index of the structural quality of graphene.

Compared with GO, the I_D/I_G ratios of the GO, rGO, GCS, and H-GCS increased from 0.93 to 1.12, 1.18, and 1.15, respectively. The increase of I_D/I_G ratios suggests the presence of defects and indicates the chemical reduction of GO [55, 56]. The obtained H-GCS resulting from the KOH heat treatment of GCS reveals a further chemical reduction of rGO oxide by decomposition of oxygen-containing functional groups. This effect can

be interpreted as an increase in high electrical conductivity of the H-GCS film and is beneficial for the application of supercapacitors. XRD was further used to analyze the phase structure of the samples (Fig. 4b). A typical peak near 10.3° (d-spacing $\sim 8.6 \text{ \AA}$) was observed for the GO sample. A broad and weak peak (002) in the XRD pattern of the rGO paper indicated the poor ordering of graphene sheets along their stacking direction, which agreed with the SEM results [57]. The peak position of GCS shifted to a lower degree compared to that of the rGO, which revealed that CSs are well intercalated between the graphene sheets as spacers. However, the (002) peak of H-GCS shifted to a lower degree after KOH activation, which indicates larger d-spacing. For H-GCS sample, the (002) XRD peak became more distinct after high temperature KOH activation process compared with the GCS samples, which suggests a higher degree of graphitization occurred in CSs during the KOH activation process. Since CSs was synthesized from glucose via hydrothermal method, the as-obtained CS exhibits amorphous carbon characteristics, which is unfavorable for electrode materials. After KOH activation process, a higher degree of graphitization of CSs in H-GCS thin film is expected to improve the electrical conductivity of the H-GCS electrode and is beneficial for its energy storage [58]. The enhanced electrical conductivity of H-GCS was verified by a standard four-point probe method. The electrical conductivity of the H-GCS electrode was measured to be 5202.9 S m^{-1} , which is much higher than that of the rGO (3673.8 S m^{-1}) and GCS (629.3 S m^{-1}) electrodes. Importantly, the sharp peak demonstrated a loose structure, which could benefit SC applications [59]. The surface chemical structure and composition of the GO, rGO, GCS, and H-GCS were further characterized by XPS measurements. The surface oxygen groups in GO were calculated as 31.09 at.%, whereas

the percentage of oxygen decreased to 11.47 at.% after treatment with hydrazine (Fig. 4c). These results demonstrate that efficient deoxygenation occurred by hydrazine reduction. Owing to the introduction of CSs into rGO sheets, the oxygen content of the GCS (13.68 at.%) was slightly higher than that of rGO. After KOH activation treatment of GCS, the percentage of oxygen in H-GCS showed a clear decline from 13.68 at.% (GCS) to 6.35 at.% (H-GCS), implying more deoxygenation of rGO sheets, which is advantageous to electrical conductivity.

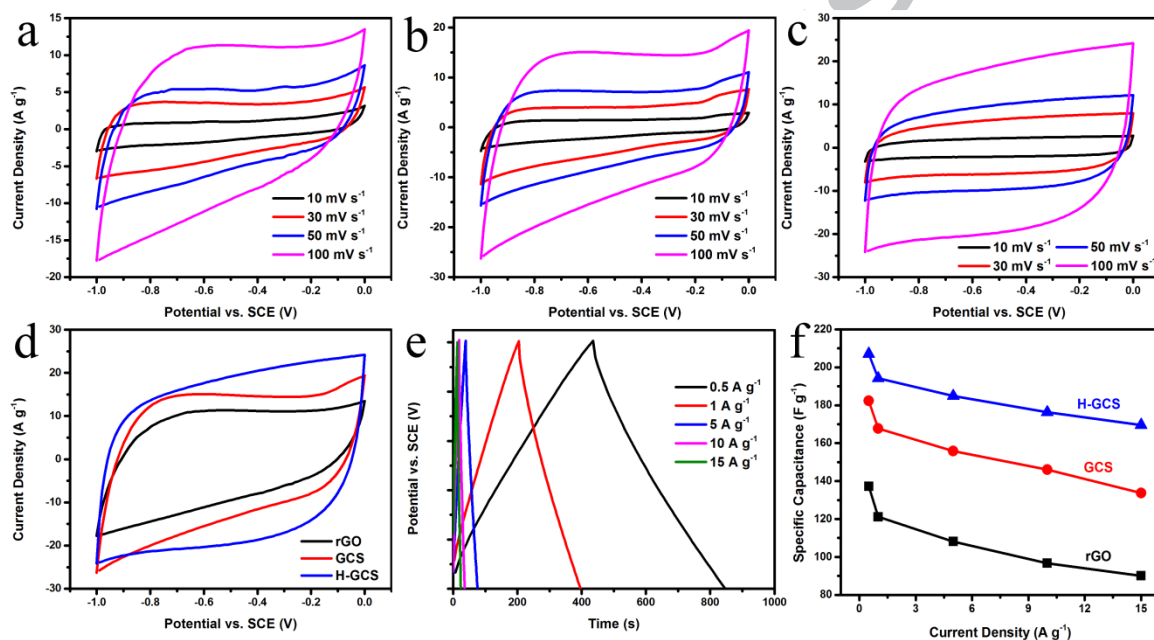


Fig. 5. Electrochemical characterization of rGO-, GCS-, and H-GCS-based film electrodes in 6.0 M KOH aqueous electrolyte. CV curves of (a) rGO, (b) GCS, and (c) H-GCS thin film electrode at the scan rates from 10 mV s^{-1} to 100 mV s^{-1} ; (d) CV curves of H-GCS compared to rGO and GCS at a scan rate of 100 mV s^{-1} ; (e) galvanostatic charge/discharge curves of H-GCS thin film; (f) Comparison of specific capacitances of rGO, GCS, and H-GCS thin-film electrodes versus various current densities.

All the as-prepared thin-film samples were directly used as freestanding electrodes to evaluate their electrochemical performance in a three-electrode system, in which a 6 M KOH aqueous solution was used as the electrolyte. CV measurements were first carried out at a sweep rate of 10, 30, 50 and 100 mV s^{-1} from -1.0 V to 0 V (Fig. 5a-d). All CV curves displayed a quasi-rectangular shape even under 100 mV s^{-1} , indicating a reversible reaction and ideal EDLC behavior. Notably, humps were observed in these CV curves of GCS, signifying the coexistence of EDLC and pseudocapacitance. The presence of pseudocapacitance is attributed to the presence of surface oxygen-containing functionalities, such as carboxylic acid groups in rGO [47, 48], as well as the abundant $-\text{OH}$ and $\text{C}=\text{O}$ groups on the surface of CSs [46]. The formation of pseudocapacitance is attributed to the following reactions for different surface oxygen functional groups [60]:



The CV curves of the H-GCS (Fig. 5c) electrode showed a more rectangular shape compared with that of the rGO (Fig. 5a) and GCS (Fig. 5b) electrodes, which indicated better capacitive performance. Obviously, the CV curves of the H-GCS electrode have higher current density and larger integral area compared with that of other samples, which revealed that H-GCS possesses superior electrochemical performance among tested samples (Fig. 5d). In addition, the H-GCS electrode retained the desirable rectangular shape for scan rates up to 100 mV s^{-1} , indicating it possesses efficient ion

transport kinetics for high rate capability. The capacitive performance of the samples was further investigated with GCD experiments at various current densities under the voltage windows of the CV measurements (Fig. 5e and S6). All samples exhibited symmetric triangular shapes in the GCD profiles, which indicated that capacitance was dominated by EDLC behavior. For the GCS electrode, a hump presented at approximately -0.1 V in the GCD indicated the presence of pseudocapacitance, which agreed well with the result obtained from CV analysis. At the current density 0.5 A g^{-1} , the specific capacitance for the H-GCS electrode was 207.1 F g^{-1} , which was higher than that of the rGO (137.3 F g^{-1}) and GCS (182.4 F g^{-1}) electrodes respectively. The results clearly show that the H-GCS electrode is capable of being charged and discharged smoothly with nearly symmetric and well-defined charge–discharge lines at different current densities. Based on the GCD curves, the specific capacitances of the H-GCS electrode were calculated as 207.1 , 194.2 , 184.9 , 176.3 , and 169.6 F g^{-1} at current densities of 0.5 , 1 , 5 , 10 , and 15 A g^{-1} , respectively. The H-GCS electrode also exhibits good capacitance retention capability (81.9%) compared with the rGO (65.6%) and GCS (73.3%) electrodes. The relationships between specific capacitance values and current densities of the samples are presented in Fig. 5f. Owing to the inadequate time for electrolyte transportation into the inner volume, the increasing current density gradually decreased the calculated specific capacitance of samples. The superb electrochemical performance could be attributed to the unique H-GCS architectures with micro-mesopores. First, the restacking of graphene sheets in H-GCS structure could be alleviated effectively to obtain higher electrochemical surface area of graphene sheets. Second, the micro-mesopores generated on the surface of the graphene sheets not only increased the electroactive sites effectively, but also facilitated

the capability of ion transport kinetics. Moreover, the H-GCS electrode exhibited better electrical conductivity than the rGO and GCS electrodes because of the higher degree of decomposition of oxygen-containing functional groups, thus preserving high electrical conductivity of the graphene sheets.

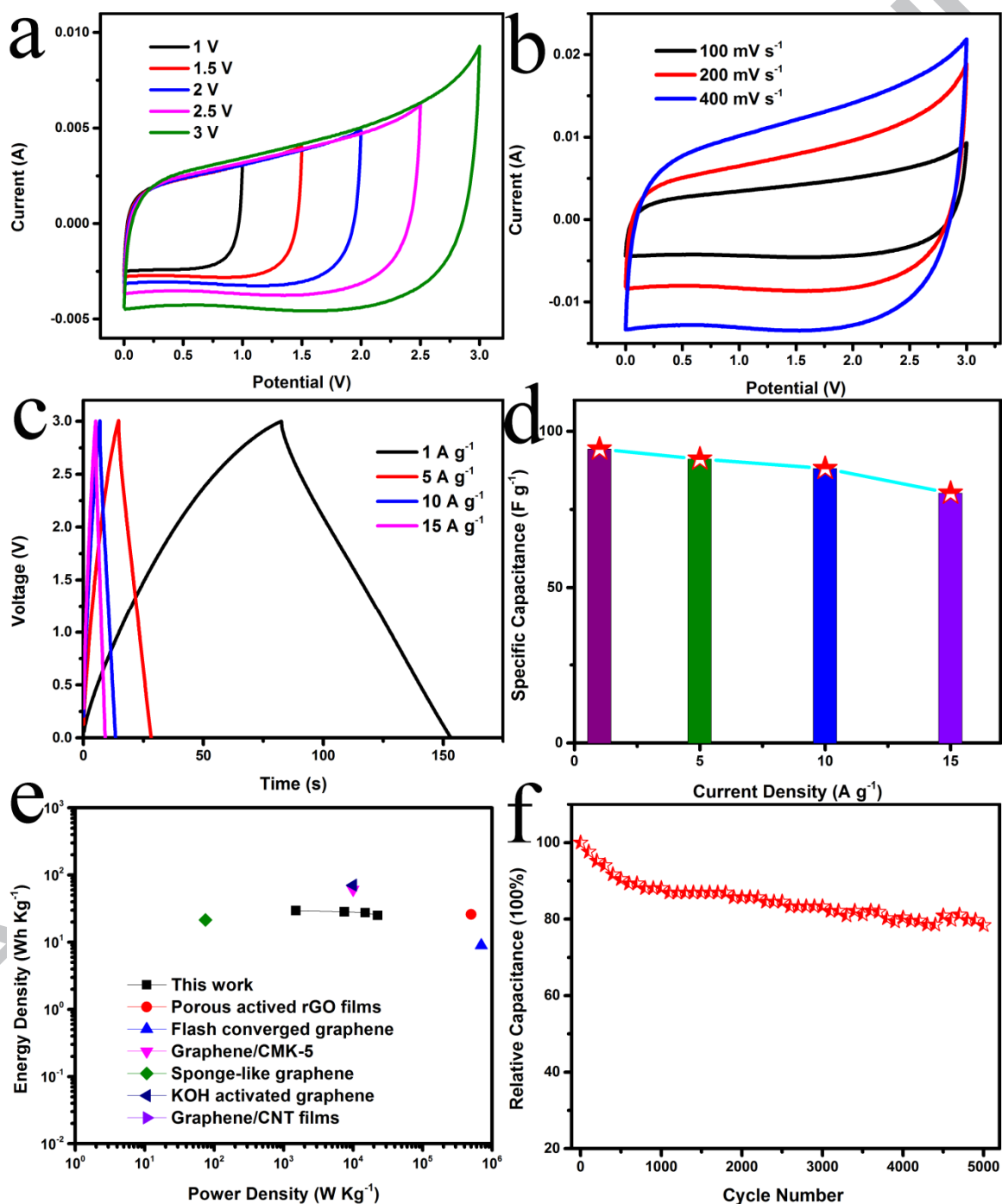


Fig. 6. Electrochemical properties of H-GCS electrode in a symmetric supercapacitor. (a) CV of H-GCS devices at 100 mV s^{-1} from 1.0 up to 3.0 V, (b) CV of H-GCS devices at various scan rates in the potential of 3.0 V, (c) Galvanostatic charge/discharge curves of H-GCS devices at different current densities, (d) Gravimetric capacitance of H-GCS electrode at various current densities, (e) Ragone plots of energy density versus power density for H-GCS devices in comparison with others reported, and (f) Cycling performance of H-GCS devices at a current density of 1.0 A g^{-1} .

To access the H-GCS electrode for practical supercapacitor application, a CR 2032 coin-cell-type device was fabricated by using the same two H-GCS electrodes with a polypropylene paper as the separator in an organic electrolyte (1 M TEABF₄ in AN). Fig. 6a exhibits the CV curves of H-GCS//H-GCS symmetric supercapacitor operated at different voltage windows at 100 mV s^{-1} . These CV curves present quasi-rectangular-shaped voltammetry characteristics with various voltage windows for 1 V to 3 V. Fig. 6b shows the CV of the H-GCS symmetric supercapacitor cycle between 0 and 3 V at various scan rates. The cell nearly retained the typical rectangular shape of CVs with slight distortion due to oxygen-related functional groups presented on the surface of H-GCS samples, as supported by the CV and GCD data. The almost symmetric charge-discharge curves (Fig. 6c) are in good agreement with their rectangular CV behavior, which indicated the dominant EDLC characteristic. Fig. 6d shows the specific capacitance of the H-GCS electrode at various current densities. Remarkably, the capacitance at 15 A g^{-1} corresponds to 78% capacitance retention relative to 1 A g^{-1} .

The device performance of the H-GCS symmetric supercapacitor was manifested in its Ragone plot (Fig. 6e). Given that the energy density of a supercapacitor is directly proportional to the square of its working voltage, the wide voltage window of TEABF₄ in AN resulted in high energy density of H-GCS symmetric supercapacitor. As shown in the Ragone plot, the H-GCS symmetric supercapacitor delivers maximum energy density of 29.5 Wh kg⁻¹ (at the power density of 1.5 kW kg⁻¹). This figure is higher than that of carbonaceous-based supercapacitor presented in literature, such as porous graphene paper symmetric SC in an organic electrolyte (1 M TEABF₄ in AN) (26 Wh kg⁻¹) [61], flash-converted graphene paper symmetric SC in an organic electrolyte (1 M TEABF₄ in AN) (9 Wh kg⁻¹) [44], pillared graphene paper symmetric SC in organic electrolyte (LiPF₄) (26 Wh kg⁻¹) [8], graphene-CMK-5 symmetric SC in organic electrolyte (LiPF₄) (26 Wh kg⁻¹) [62], and sponge-like graphene symmetric SC in ionic liquid (21.4 Wh kg⁻¹) [63]. Even at a power density of 22.6 kW kg⁻¹, the cell delivered high energy density of 25.1 Wh kg⁻¹. Remarkably, the cycle stability of H-GCS device retained 79% of the initial specific capacitance after 5000 cycles at a current density of 1.0 A g⁻¹ (Fig. 6f). The fading of the capacitance is tightly related with the decomposition of the organic electrolyte on the active surface of the electrode. The organic electrolyte is decomposed on the electrode materials, which lead to changes of their chemical composition [64]. The gases including methane, ethane, di-oxygen, and di-hydrogen are the main forming products. These decomposition productions can be trapped in the pores, leading to a decrease of accessible porosity. And the evolved gasses are expected to be blocked in the pores of separator and active electrodes, giving rise to a resistance increase and the hindrance of ion diffusion.

4. Conclusion

A novel approach is reported for preparing a high-conductivity and porous H-GCS film electrode consisting of CSs intercalated between holey rGO sheets via robust electrostatic self-assembly, vacuum filtration, and subsequent KOH activation. Owing to the pillared structure, micro-mesopores on rGO sheets, improved electrical conductivity, efficient electron transport pathways, and rapid ion diffusion kinetics, the freestanding H-GCS paper electrode exhibits large reversible capacity, high rate capability, high energy density, and great cycling stability. This study provides an effective approach to alleviate the aggregation and restacking issue of graphene electrodes for high-performance energy storage devices.

Acknowledgements

This work was supported by the Global Frontier hybrid Interface Materials (GFHIM) program of the National Research Foundation of Korea (NRF) funded by the Ministry of Science, ICT & Future Planning (2013M3A6B1078874), the Science and Technology Development Fund from Macau SAR (FDCT-098/2015/A3), and the Start-up Research Grant (SRG2015-00057-FST) from Research & Development Office at University of Macau.

References

- [1] B. Dunn, H. Kamath, J.M. Tarascon, Electrical energy storage for the grid: a battery of choices, *Science* 334 (2011) 928-935.

- [2] X.P. Zhuang, K.F. Jia, B.W. Cheng, X. Feng, S.J. Shi, B. Zhang, Solution blowing of continuous carbon nanofiber yarn and its electrochemical performance for supercapacitors, *Chem. Eng. J.* 237 (2014) 308-311.
- [3] Z.B. Lei, N. Christov, X.S. Zhao, Intercalation of mesoporous carbon spheres between reduced graphene oxide sheets for preparing high-rate supercapacitor electrodes, *Energy Environ. Sci.* 4 (2011) 1866-1873.
- [4] C. Ma, Y.J. Li, J.L. Shi, Y. Song, L. Liu, High-performance supercapacitor electrodes based on porous flexible carbon nanofiber paper treated by surface chemical etching, *Chem. Eng. J.* 249 (2014) 216-225.
- [5] K. Liu, C.A. Wang, Honeycomb-alumina supported garnet membrane: composite electrolyte with low resistance and high strength for lithium metal batteries, *J. Power Sources* 281 (2015) 399-403.
- [6] S. Li, C.A. Wang, Design and synthesis of hierarchically porous MnO₂/carbon hybrids for high performance electrochemical capacitors, *J. Colloid Interf. Sci.* 438 (2015) 61-67.
- [7] M.J. Deng, C.Z. Song, C.C. Wang, Y.C. Tseng, J.M. Chen, K.T. Lu, Low cost facile synthesis of large-area cobalt hydroxide nanorods with remarkable pseudocapacitance, *ACS Appl. Mater. Interfaces* 7 (2015) 9147-9156.
- [8] G.K. Wang, X. Sun, F.Y. Lu, H.T. Sun, M.P. Yu, W.L. Jiang, C.S. Liu, J. Lian, Flexible pillared graphene-paper electrodes for high-performance electrochemical supercapacitors, *Small* 8 (2012) 452-459.

- [9] Shuxing Wu, S. H. Hui, K. N. Hui, K. H. Kim, Ultrathin porous NiO nanoflake arrays on nickel foam as an advanced electrode for high performance asymmetric supercapacitors, *J. Mater. Chem. A* 4 (2016) 9113-9123.
- [10] K.S. Novoselov, A.K. Geim, S.V. Morozov, D. Jiang, Y. Zhang, S.V. Dubonos, I.V. Grigorieva, A.A. Firsov, Electric field effect in atomically thin carbon films, *Science* 306 (2004) 666-669.
- [11] Y.P. Zhai, Y.Q. Dou, D.Y. Zhao, P.F. Fulvio, R.T. Mayes, S. Dai, Carbon materials for chemical capacitive energy storage, *Adv. Mater.* 23 (2011) 4828-4850.
- [12] Y.Q. Sun, Q.O. Wu, G.Q. Shi, Graphene based new energy materials, *Energy Environ. Sci.* 4 (2011) 1113-1132.
- [13] C.G. Liu, Z.N. Yu, D. Neff, A. Zhamu, B.Z. Jang, Graphene-based supercapacitor with an ultrahigh energy density, *Nano Letters* 10 (2010) 4863-4868.
- [14] J.L. Xia, F. Chen, J.H. Li, N.J. Tao, Measurement of the quantum capacitance of graphene, *Nat. Nanotechnol.* 4 (2009) 505-509.
- [15] M. Segal, Selling graphene by the ton, *Nat. Nanotechnol.* 4 (2009) 611-613.
- [16] Y. Zhu, L. Li, C.G. Zhang, G. Casillas, Z.Z. Sun, Z. Yan, G.D. Ruan, Z.W. Peng, A.R.O. Raji, C. Kittrell, R.H. Hauge, J.M. Tour, A seamless three-dimensional carbon nanotube graphene hybrid material, *Nat. Commun.* 3 (2012) 1225.
- [17] F.D. Novaes, R. Rurali, P. Ordejon, Electronic transport between graphene layers covalently connected by carbon nanotubes, *ACS Nano* 4 (2010) 7596-7602.
- [18] S.J. Guo, S.J. Dong, Graphene nanosheet: synthesis, molecular engineering, thin film, hybrids, and energy and analytical applications, *Chem. Soc. Rev.* 40 (2011) 2644-2672.

- [19] B.G. Choi, S.J. Chang, Y.B. Lee, J.S. Bae, H.J. Kim, Y.S. Huh, 3D heterostructured architectures of Co_3O_4 nanoparticles deposited on porous graphene surfaces for high performance of lithium ion batteries, *Nanoscale* 4 (2012) 5924-5930.
- [20] J.Y. Luo, H.D. Jang, J.X. Huang, Effect of sheet morphology on the scalability of graphene-based ultracapacitors, *ACS Nano* 7 (2013) 1464-1471.
- [21] R.O. Brennan, The Interlayer Binding in Graphite, *J. Chem. Phys* 20 (1952) 40-48.
- [22] C.Y. Chen, C.Y. Fan, M.T. Lee, J.K. Chang, Tightly connected MnO_2 -graphene with tunable energy density and power density for supercapacitor applications, *J. Mater. Chem.* 22 (2012) 7697-7700.
- [23] J. Chang, S. Adhikari, T.H. Lee, B. Li, F. Yao, D.T. Pham, V.T. Le, Y.H. Lee, Leaf vein-inspired nanochanneled graphene film for highly efficient micro-supercapacitors, *Adv. Energy Mater.* 5 (2015) 1500003.
- [24] Y.J. Zou, Q.Y. Wang, C.L. Xiang, Z. She, H.L. Chu, S.J. Qiu, F. Xu, S.S. Liu, C.Y. Tang, L.X. Sun, One-pot synthesis of ternary polypyrrole-prussian-blue-graphene-oxide hybrid composite as electrode material for high-performance supercapacitors, *Electrochim Acta* 188 (2016) 126-134.
- [25] W.J. Ma, S.H. Chen, S.Y. Yang, W.P. Chen, Y.H. Cheng, Y.W. Guo, S.J. Peng, S. Ramakrishna, M.F. Zhu, Hierarchical MnO_2 nanowire/graphene hybrid fibers with excellent electrochemical performance for flexible solid-state supercapacitors, *J. Power Sources* 306 (2016) 481-488.
- [26] F. Yang, M.W. Xu, S.J. Bao, H. Wei, H. Chai, Self-assembled hierarchical graphene/polyaniline hybrid aerogels for electrochemical capacitive energy storage, *Electrochim Acta* 137 (2014) 381-387.

- [27] H.L. Wang, H.S. Casalongue, Y.Y. Liang, H.J. Dai, Ni(OH)₂ nanoplates grown on graphene as advanced electrochemical pseudocapacitor materials, *J. Am. Chem. Soc.* 132 (2010) 7472-7477.
- [28] D. Zhu, Y. Wang, G. Yuan, H. Xia, High-performance supercapacitor electrodes based on hierarchical Ti@MnO₂ nanowire arrays, *Chem. Commun.* 50 (2014) 2876-2878.
- [29] Q. Wu, Y.X. Xu, Z.Y. Yao, A.R. Liu, G.Q. Shi, Supercapacitors based on flexible graphene/polyaniline nanofiber composite films, *ACS Nano* 4 (2010) 1963-1970.
- [30] S.X. Wu, K.S. Hui, K.N. Hui, One-dimensional core-shell architecture composed of silver nanowire@hierarchical nickel-aluminum layered double hydroxide nanosheet as advanced electrode materials for pseudocapacitor, *J. Phys. Chem. C* 119 (2015) 23358-23365.
- [31] Y. Liu, X.Y. Cai, B.F. Luo, M. Yan, J.H. Jiang, W.D. Shi, MnO₂ decorated on carbon sphere intercalated graphene film for high-performance supercapacitor electrodes, *Carbon* 107 (2016) 426-432.
- [32] S. Wu, K.S. Hui, K.N. Hui, K.H. Kim, Electrostatic-induced assembly of graphene-encapsulated carbon@nickel-aluminum layered double hydroxide core-shell spheres hybrid structure for high-energy and high-power-density asymmetric supercapacitor, *ACS Appl. Mater. Interfaces* 9 (2017) 1395-1406.
- [33] V. Sridhar, H.J. Kim, J.H. Jung, C. Lee, S. Park, I.K. Oh, Defect-engineered three-dimensional graphene-nanotube-palladium nanostructures with ultrahigh capacitance, *ACS Nano* 6 (2012) 10562-10570.

- [34] F. Du, D.S. Yu, L.M. Dai, S. Ganguli, V. Varshney, A.K. Roy, Preparation of tunable 3D pillared carbon nanotube-graphene networks for high-performance capacitance, *Chem. Mater.* 23 (2011) 4810-4816.
- [35] N. Jung, S. Kwon, D. Lee, D.M. Yoon, Y.M. Park, A. Benayad, J.Y. Choi, J.S. Park, Synthesis of chemically bonded graphene/carbon nanotube composites and their application in large volumetric capacitance supercapacitors, *Adv. Mater.* 25 (2013) 6854-6858.
- [36] D.S. Yu, L.M. Dai, Self-assembled graphene/carbon nanotube hybrid films for supercapacitors, *J. Phys. Chem. Lett.* 1 (2010) 467-470.
- [37] D.T. Pham, T.H. Lee, D.H. Luong, F. Yao, A. Ghosh, V.T. Le, T.H. Kim, B. Li, J. Chang, Y.H. Lee, Carbon nanotube-bridged graphene 3D building blocks for ultrafast compact supercapacitors, *ACS Nano* 9 (2015) 2018-2027.
- [38] Z.B. Lei, J.T. Zhang, L.L. Zhang, N.A. Kumar, X.S. Zhao, Functionalization of chemically derived graphene for improving its electrocapacitive energy storage properties, *Energy Environ. Sci.* 9 (2016) 1891-1930.
- [39] C.X. Guo, C.M. Li, A self-assembled hierarchical nanostructure comprising carbon spheres and graphene nanosheets for enhanced supercapacitor performance, *Energy Environ. Sci.* 4 (2011) 4504-4507.
- [40] X.T. Xu, Y. Liu, M. Wang, C. Zhu, T. Lu, R. Zhao, L.K. Pan, Hierarchical hybrids with microporous carbon spheres decorated three-dimensional graphene frameworks for capacitive applications in supercapacitor and deionization, *Electrochim Acta* 193 (2016) 88-95.

- [41] Y.Y. Li, Z.S. Li, P.K. Shen, Simultaneous formation of ultrahigh surface area and three-dimensional hierarchical porous graphene-like networks for fast and highly stable supercapacitors, *Adv. Mater.* 25 (2013) 2474-2480.
- [42] W.S. Hummers, R. E. Offeman, Preparation of graphitic oxide, *J. Am. Chem. Soc.* 80 (1958) 1339.
- [43] N.I. Kovtyukhova, P.J. Ollivier, B.R. Martin, T.E. Mallouk, S.A. Chizhik, E.V. Buzaneva, A.D. Gorchinskiy, Layer-by-layer assembly of ultrathin composite films from micron-sized graphite oxide sheets and polycations, *Chem. Mater.* 11 (1999) 771-778.
- [44] L.J. Wang, M.F. El-Kady, S. Dubin, J.Y. Hwang, Y.L. Shao, K. Marsh, B. McVerry, M.D. Kowal, M.F. Mousavi, R.B. Kaner, Flash converted graphene for ultra-high power supercapacitors, *Adv. Energy Mater.* 5 (2015) 1500786.
- [45] Y.Q. Yang, R.Q. Pang, X.J. Zhou, Y.J. Zhang, H.X. Wu, S.W. Guo, Composites of chemically-reduced graphene oxide sheets and carbon nanospheres with three-dimensional network structure as anode materials for lithium ion batteries, *J. Mater. Chem.* 22 (2012) 23194-23200.
- [46] L. Fan, L. Tang, H.F. Gong, Z.H. Yao, R. Guo, Carbon-nanoparticles encapsulated in hollow nickel oxides for supercapacitor application, *J. Mater. Chem.* 22 (2012) 16376-16381.
- [47] S. Stankovich, D.A. Dikin, R.D. Piner, K.A. Kohlhaas, A. Kleinhammes, Y. Jia, Y. Wu, S.T. Nguyen, R.S. Ruoff, Synthesis of graphene-based nanosheets via chemical reduction of exfoliated graphite oxide, *Carbon* 45 (2007) 1558-1565.
- [48] D. Li, M.B. Muller, S. Gilje, R.B. Kaner, G.G. Wallace, Processable aqueous dispersions of graphene nanosheets, *Nat. Nanotechnol.* 3 (2008) 101-105.

- [49] T.A. Gschneidtner, Y.A.D. Fernandez, S. Syrenova, F. Westerlund, C. Langhammer, K. Moth-Poulsen, A versatile self-assembly strategy for the synthesis of shape-selected colloidal noble metal nanoparticle heterodimers, *Langmuir* 30 (2014) 3041-3050.
- [50] M.A. Lillo-Rodenas, D. Cazorla-Amoros, A. Linares-Solano, Understanding chemical reactions between carbons and NaOH and KOH - An insight into the chemical activation mechanism, *Carbon* 41 (2003) 267-275.
- [51] M. Sevilla, A.B. Fuertes, A general and facile synthesis strategy towards highly porous carbons: carbonization of organic salts, *J. Mater. Chem. A* 1 (2013) 13738-13741.
- [52] S.Y. Wang, B. Pei, X.S. Zhao, R.A.W. Dryfe, Highly porous graphene on carbon cloth as advanced electrodes for flexible all-solid-state supercapacitors, *Nano Energy* 2 (2013) 530-536.
- [53] M. Kim, I. Oh, J. Kim, Porous silicon carbide flakes derived from waste silicon wafer for electrochemical supercapacitor, *Chem. Eng. J.* 289 (2016) 170-179.
- [54] A.C. Ferrari, J. Robertson, Interpretation of raman spectra of disordered and amorphous carbon, *Phys. Rev. B* 61 (2000) 14095-14107.
- [55] T.T. Li, N. Li, J.W. Liu, K. Cai, M.F. Foda, X.M. Lei, H.Y. Han, Synthesis of functionalized 3D porous graphene using both ionic liquid and SiO₂ spheres as "spacers" for high-performance application in supercapacitors, *Nanoscale* 7 (2015) 659-669.
- [56] Z. Bo, W.G. Zhu, W. Ma, Z.H. Wen, X.R. Shuai, J.H. Chen, J.H. Yan, Z.H. Wang, K.F. Cen, X.L. Feng, Vertically oriented graphene bridging active-layer/current-collector interface for ultrahigh rate supercapacitors, *Adv. Mater.* 25 (2013) 5799-5806.
- [57] H.B. Feng, R. Cheng, X. Zhao, X.F. Duan, J.H. Li, A low-temperature method to produce highly reduced graphene oxide, *Nat. Commun.* 4 (2013) 1539-1546.

- [58] H.J. Liu, W.J. Cui, L.H. Jin, C.X. Wang, Y.Y. Xia, Preparation of three-dimensional ordered mesoporous carbon sphere arrays by a two-step templating route and their application for supercapacitors, *J. Mater. Chem.* 19 (2009) 3661-3667.
- [59] J. Yan, Q. Wang, T. Wei, L.L. Jiang, M.L. Zhang, X.Y. Jing, Z.J. Fan, Template-assisted low temperature synthesis of functionalized graphene for ultrahigh volumetric performance supercapacitors, *ACS Nano* 8 (2014) 4720-4729.
- [60] Y. Fang, B. Luo, Y.Y. Jia, X.L. Li, B. Wang, Q. Song, F.Y. Kang, L.J. Zhi, Renewing functionalized graphene as electrodes for high-performance supercapacitors, *Adv. Mater.* 24 (2012) 6348-6355.
- [61] Y. Song, J. Wang, Z. Li, D. Guan, T. Mann, Q. Liu, M. Zhang, L. Liu, Self-assembled hierarchical porous layered double hydroxides by solvothermal method and their application for capacitors, *Micropor. Mesopor. Mat.* 148 (2012) 159-165.
- [62] Z.B. Lei, Z.H. Liu, H.J. Wang, X.X. Sun, L. Lu, X.S. Zhao, A high-energy-density supercapacitor with graphene-CMK-5 as the electrode and ionic liquid as the electrolyte, *J. Mater. Chem. A* 1 (2013) 2313-2321.
- [63] Z.W. Xu, Z. Li, C.M.B. Holt, X.H. Tan, H.L. Wang, B.S. Amirkhiz, T. Stephenson, D. Mitlin, Electrochemical supercapacitor electrodes from sponge-like graphene nanoarchitectures with ultrahigh power density, *J. Phys. Chem. Lett.* 3 (2012) 2928-2933.
- [64] P. Azais, L. Duclaux, P. Florian, D. Massiot, M.A. Lillo-Rodenas, A. Linares-Solano, J.P. Peres, C. Jehoulet, F. Beguin, Causes of supercapacitors ageing in organic electrolyte, *J. Power Sources* 171 (2007) 1046-1053.

Figure captions

Scheme 1 Schematic illustration of the carbon sphere-intercalated holey graphene 3D heterostructured architectures. Electrostatic attractive interactions between negatively charged rGO sheets and positively charged CTAB-grafted carbon spheres render the formation of 3D heterostructured architectures. KOH activation produces microscale pores in the graphene layers, which are expected to provide rapid ion diffusion path.

Fig. 1. (a) SEM images of CSs and (b) Tapping mode AFM image of GO sheets deposited on SiO₂ substrate.

Fig. 2. Schematic illustration and cross-sectional SEM images of (a) rGO, (b), GCS, and (c) H-GCS thin films. (a) Original rGO thin film without CSs. The individual rGO sheets are prone to self-restacking because of the van der Waals interactions, leading to the inferior migration behavior of electrolyte ions between the restacked rGO sheets. (b) rGO sheets intercalated by CS with large inter-layer voids, leaving more diffusion pathways for electrolyte ions. (c) Holes in the pillared rGO sheets can function as the ion transport pathways to speed up ion migration through the entire H-GCS film.

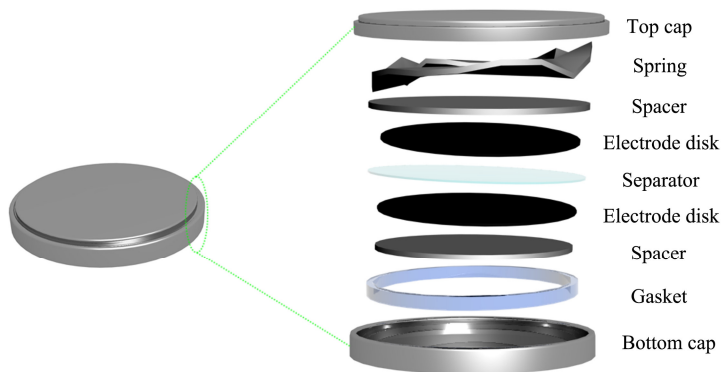
Fig. 3. Top-view SEM images of rGO (a and b) and GCS (c and d), and TEM images of H-GCS (e and f) thin films.

Fig. 4. (a) Raman spectra, (b) XRD patterns and (c) XPS spectra of GO, rGO, GCS, and H-GCS.

Fig. 5. Electrochemical characterization of rGO-, GCS-, and H-GCS-based film electrodes in 6.0 M KOH aqueous electrolyte. CV curves of (a) rGO, (b) GCS, and (c) H-GCS thin film electrode at the scan rates from 10 mV s⁻¹ to 100 mV s⁻¹; (d) CV curves

of H-GCS compared to rGO and GCS at a scan rate of 100 mV s^{-1} ; (e) galvanostatic charge/discharge curves of H-GCS thin film; (f) Comparison of specific capacitances of rGO, GCS, and H-GCS thin-film electrodes versus various current densities.

Fig. 6. Electrochemical properties of H-GCS electrode in a symmetric supercapacitor. (a) CV of H-GCS devices at 100 mV s^{-1} from 1.0 up to 3.0 V, (b) CV of H-GCS devices at various scan rates in the potential of 3.0 V, (c) Galvanostatic charge/discharge curves of H-GCS devices at different current densities, (d) Gravimetric capacitance of H-GCS electrode at various current densities, (e) Ragone plots of energy density versus power density for H-GCS devices in comparison with others reported, and (f) Cycling performance of H-GCS devices at a current density of 1.0 A g^{-1} .



ACCEPTED MANUSCRIPT

Highlights

- Self-assembly of holey graphene sheets intercalates with carbon spheres.
- The film electrode exhibits 207.1 F g^{-1} of specific capacitance.
- Maximum specific energy and power of 29.5 Wh kg^{-1} and 22.6 kW kg^{-1} are achieved.

ACCEPTED MANUSCRIPT